Nanoscale

PAPER

View Article Online
View Journal | View Issue

Check for updates

Cite this: *Nanoscale*, 2017, **9**, 7104

Strong enhancement of electrical conductivity in two-dimensional micrometer-sized RuO_2 nanosheets for flexible transparent electrodes†

Somi Yoo,‡[a] Jeongmin Kim,‡[a] Hongjae Moon,[a] Se Yun Kim,[b] Dong-su Ko,[c] Weon Ho Shin,[b] Sungwoo Hwang,[b] Doh Won Jung,[b] Soohwan Sul,[c] Chan Kwak,[b] Jong Wook Roh*[b] and Wooyoung Lee *[a]

Received 24th December 2016,
Accepted 26th April 2017

DOI: 10.1039/c6nr09894k

rsc.li/nanoscale

The enhancement in electrical transport properties of exfoliated individual RuO_2 NSs was systemically investigated for their application in flexible electronics and optoelectronics. Decoration of Ag NPs on the surface of the RuO_2 NSs provides donor electrons and dramatically increases the electrical conductivity of the monolayer RuO_2 NSs by up to 3700%. The n-type doping behavior was confirmed *via* Hall measurement analysis of the doped RuO_2 NSs. The layer number- and temperature-dependence of the conductivity were also investigated. Moreover, carrier concentration and mobility were obtained from Hall measurements, indicating that the undoped RuO_2 NSs had ambipolar transport and semi-metallic characteristics. Moreover, the Ag-doped RuO_2 NS multilayer films on polycarbonate substrates were demonstrated by the Langmuir–Blodgett assembly methods, showing one-third reduction in the sheet resistance and extraordinarily high bending stability that the change in the resistance was less than 1% over 50 000 cycles.

Published on 28 April 2017. Downloaded by Yonsei University on 09/08/2017 07:25:42.

Introduction

Since the discovery of graphene,[1,2] two-dimensional (2D) inorganic materials have been of significant interest in the fields of atomic electronics,[3–5] photonics,[6,7] and flexible electronics[8–10] due to their unique dimensionality, atomic-scale thickness, and flatness. Due to these intriguing physical properties and the wide range of applications of 2D materials, a number of studies have been carried out on other 2D materials such as hexagonal boron nitride (hBN)[11] and transition metal dichalcogenides (TMDCs: MoS_2, $MoSe_2$, WS_2, $NbSe_2$, $TaSe_2$, *etc.*),[12–17] as well as on 2D oxide materials (such as TiO_2, MnO_2, V_2O_5, *etc.*).[18–21] In particular, the 2D oxide materials have been suggested as promising transparent electrode materials due to their high flexibility, unique optical properties, and stability under ambient conditions. These merits lay the foundation for viable atomic electronics, using 2D oxide materials as transparent electrode materials. However, the poor electrical properties of 2D oxide materials, which are mostly caused by low carrier mobility (μ), as compared to those of the corresponding bulk structures constitute the main hurdle for realizing transparent electrodes using 2D oxide materials.

Rutile-type ruthenium oxide (RuO_2) is of a special technological interest due to its thermodynamic stability, semi-transparency, and distinctive metallic properties. The Fermi level of RuO_2 is positioned in the middle of a conduction band that is primarily encompassed by Ru-4d orbitals,[22] typically showing metallic behavior with a single-crystalline resistivity of 35.2 μΩ cm.[23] Moreover, rutile-type RuO_2 has a layered structure, which is advantageous for the easy fabrication of nanosheets (NSs) *via* exfoliation. For example, the sheet resistance of single-layer RuO_2 NSs synthesized *via* electrostatic self-assembly was measured to be approximately 12 kΩ sq^{-1}, which was relatively high for electrodes, as observed *via* scanning probe microscopy.[24] Wang *et al.* obtained a sheet resistance of 4.1 and 0.9 kΩ sq^{-1} for two- and five-layered RuO_2 NSs films at room temperature, respectively; however, most of their studies have been focused on all-NS ultrathin capacitors.[25] Although the electrical characteristics of RuO_2 NSs are of critical importance in predicting the feasibility of applying RuO_2 NSs to atomic-layer devices, to date, electrical properties such as

[a]*Department of Materials Science and Engineering Yonsei University, 50 Yonsei-ro, Seodaemoon-gu, Seoul 03722, Republic of Korea. E-mail: wooyoung@yonsei.ac.kr*
[b]*Inorganic Materials Lab, Samsung Advanced Institute of Technology, Samsung Electronics, 130 Samsung-ro, Suwon-si, Gyeonggi-do, 16678, Republic of Korea. E-mail: jw.roh@samsung.com*
[c]*Platform Technology Lab, Samsung Advanced Institute of Technology, Samsung Electronics, 130 Samsung-ro, Suwon-si, Gyeonggi-do, 16678, Republic of Korea*
†Electronic supplementary information (ESI) available. See DOI: 10.1039/c6nr09894k
‡These authors contributed equally to this work.

This journal is © The Royal Society of Chemistry 2017

Published on 28 April 2017. Downloaded by Yonsei University on 09/08/2017 07:25:42.

carrier concentration and mobility have not been studied in individual monolayer RuO_2 NSs.

Herein, we proposed an easy method for enhancing the electrical conductivity *via* doping RuO_2 NSs with Ag nanoparticles (NPs), which dramatically increased the electrical conductivity of monolayer RuO_2 NSs by up to 3700%. This result indicates that the electrical properties can be modulated *via* the decoration of metal NPs on the surface of RuO_2 NSs. In addition, we firstly performed a systematic study on the layer number-dependent electrical conductivities of individual pristine RuO_2 NSs and Ag-doped RuO_2 NSs *via* a four-probe measurement technique; it was observed that electrical transport through individual RuO_2 NSs was limited by the surface scattering of electrons. Moreover, transparent conductive films, which were deposited layer-by-layer on a polycarbonate substrate by the Langmuir–Blodgett (LB) assembly method, were fabricated using the Ag-doped RuO_2 NSs with the lateral sizes ranging from a few to ~10 μm. This result demonstrates the feasibility of using 2D oxide materials as transparent electrodes in flexible electronics and optoelectronics.

Experimental

Synthesis and exfoliation of RuO_2 NSs

Exfoliation of layered alkali metal ruthenates was employed to synthesize RuO_2 NSs, as shown in Fig. 1a.[24,25] Potassium ruthenates were produced by annealing a mixture of potassium carbonate (K_2CO_3, >99.0%, Aldrich) and ruthenium dioxide (RuO_2, 99.9%, Aldrich). K_2CO_3 and RuO_2 were calcined at 500 °C for 6 hours. After calcination, K_2CO_3 and RuO_2 were mixed in a 5 : 8 molar ratio and annealed at 900 °C under N_2 with a flow rate of 2 L min^{-1} for 24 hours using a furnace. Then, the annealed compounds were ground to fine powder using an agate mortar and washed with 1 L deionized water (obtained by an 18 MΩ system) under magnetic stirring at room temperature for 24 hours to acquire the potassium ruthenates with the composition of $K_xRuO_{2.1}{\cdot}nH_2O$ ($0 < x \leq 0.3$). After washing, potassium ruthenates with the lateral sizes over 1 mm were obtained. Potassium ions were exchanged with protons by immersing the potassium ruthenates in 1 M hydrochloric acid (HCl, 35%, Samchun Chemicals) for 3 days at 60 °C. As shown in the field emission scanning electron microscopy (FE-SEM, FEI Nova 450) images in Fig. 1b, the layers were clearly separated in the protonic-layered ruthenates after the proton exchange reaction. The acid-treated protonic-layered ruthenates were exfoliated *via* the intercalation of tetrabutylammonium hydroxide (TBAOH, 99.0%, Aldrich) solution (40 wt% in H_2O). The TBAOH solution containing the protonic-layered ruthenates was gently stirred for 2 weeks at room temperature. After finishing the exfoliation, RuO_2 NSs were obtained *via* centrifuging (2000 rpm, 60 min) and stably suspended in deionized water, as shown in Fig. 1c.

Exfoliation of the layered structure into individual nanosheets was confirmed *via* high-resolution transmission electron microscopy (HR-TEM, FEI Titan Cubed) and atomic force microscopy (AFM, JPK Instruments Nanowizard 1). The TEM image, as depicted in Fig. 1d, clearly shows that the exfoliated RuO_2 NSs have a smooth surface without the wrinkled surface texture and are well separated from other RuO_2 NSs without aggregation. The monolayer RuO_2 NSs were measured using AFM and found to be approximately 1 nm thick with a lateral size of more than 8 μm, as shown in Fig. 1e. The measured thickness was close to the theoretical thickness of the nanosheets.[23] The optical transmittance of an individual RuO_2 NS was measured to be approximately 98.4% and 96.2%

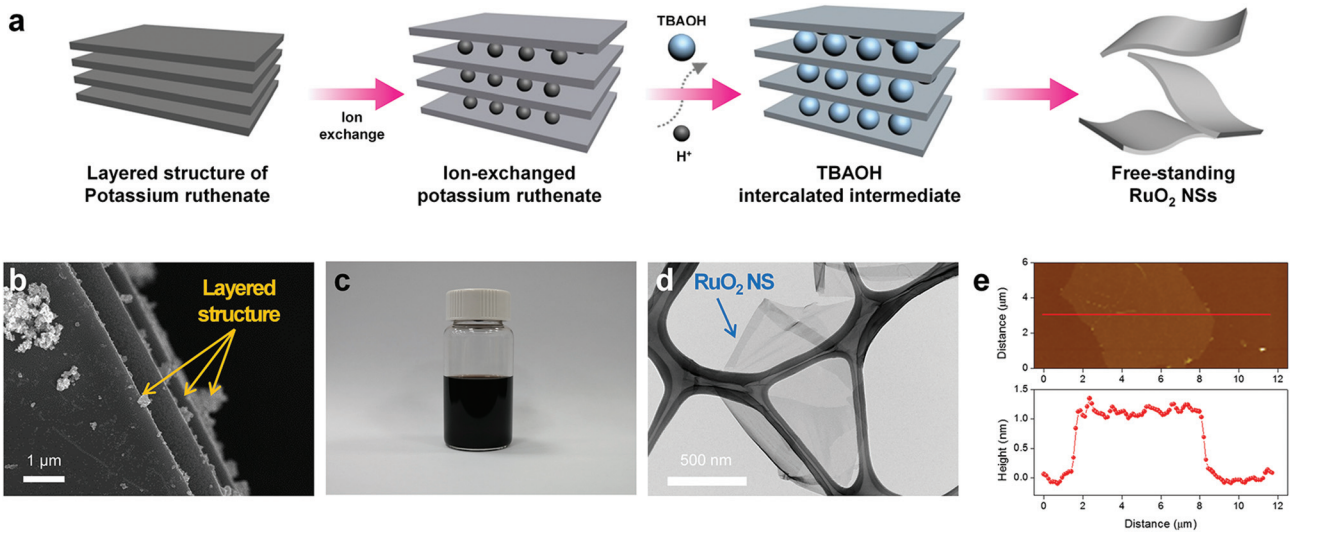

Fig. 1 (a) Schematic of the exfoliation process from the bulk RuO_2-layered structure to the corresponding monolayered NSs. (b) The SEM image of the layered structure of the acid-treated protonic-layered ruthenates. (c) Image of RuO_2 NS suspensions. (d) TEM image of the exfoliated RuO_2 NS on the Cu grid. (e) Topographic AFM image of the monolayered RuO_2 NS dispersed on a Si/SiO_2 substrate (up) and the height profile of the corresponding monolayered RuO_2 NS.

Published on 28 April 2017. Downloaded by Yonsei University on 09/08/2017 07:25:42.

for monolayer and two-layered nanosheets, respectively, in the visible region at the wavelength (λ) of 400–700 nm *via* a UV-Vis absorption spectrometer capable of microscopic characterization (QDI 2010, Craic Technologies Inc.) (Fig. S1†). Note that this value is higher than that of single-layer chemical vapor-deposited (CVD) graphene.[26]

Characterization of the Ag-doped RuO_2 NSs

For the enhancement of the electrical conductivity, metal doping on the RuO_2 NSs was carried out by decorating Ag NPs on the surfaces of the RuO_2 NSs. The decoration of Ag NPs was conducted by immersing the RuO_2 NSs in a 0.05 M Ag-acetate (CH_3COOAg, >99%, Aldrich) solution for 2 days at room temperature. After immersion, the extra Ag NPs on the surfaces of the RuO_2 NSs were removed by dipping the samples in deionized water. To reduce the number of silver oxide (AgO_x) NPs on the surfaces of the RuO_2 NSs, which were formed as a by-product of the Ag-acetate solution treatment, the samples were placed in a 0.05 M sodium borohydride ($NaBH_4$, >99.99%, Aldrich) solution for 2 min. The TEM images (Fig. 2a–c) show the surface of a Ag-doped RuO_2 NS on the TEM grid with different resolutions; the images prove that the Ag NPs were well dispersed on the surface. HR-TEM image in Fig. 2c shows that the average diameters of the Ag NPs were 2–3 nm. TEM energy dispersive X-ray spectroscopy (TEM-EDX, Super-XTM XEDS detector) pattern, as shown in Fig. 2d, clearly shows Ag NPs absorbed on the surface of the RuO_2 NS. Fig. 2e shows the topographic AFM image of a Ag-doped RuO_2 NS dispersed on a Si/SiO_2 substrate, revealing that the Ag NPs are only decorated on the RuO_2 NSs. It was expected that the Ag NPs were located at the defect sites on the surface, bonding with the oxygen atoms of RuO_2 NSs and providing donor electrons to RuO_2 NSs.

Device fabrication and transport characterization

The electron-beam lithography (EBL, JSM-7001F JEOL and ELPHY Quantum Raith) method was employed for the fabrication of individual RuO_2 NS devices. Prior to dispersing the RuO_2 NSs by drop-casting on thermally oxidized Si (100) substrates, where the alignment markers were patterned for EBL, the surface of the substrates were exposed for 30 minutes *via* ultra violet(UV)-ozone treatment to obtain hydrophilic surface. The electrodes of Cr (5 nm)/Au (50 nm) were deposited using an ultra-high vacuum sputtering system (custom-made). The resistances (R) of individual RuO_2 NS devices were measured using the combination of National Instruments Labview software and I–V measurement system (Keithley Model nanovoltmeter 2182A and 236). The conductivities were calculated from R by the relation, $\sigma = 1/\rho = L/(Rtw)$, where L, t, and w are the length, thickness, and width, respectively. The temperature-dependent resistances were obtained in the temperature range of 10–300 K using a closed cycle cryostat. All measurements were carried out in a high vacuum of less than 5×10^{-6} Torr to eliminate convectional thermal fluctuation. The thickness of

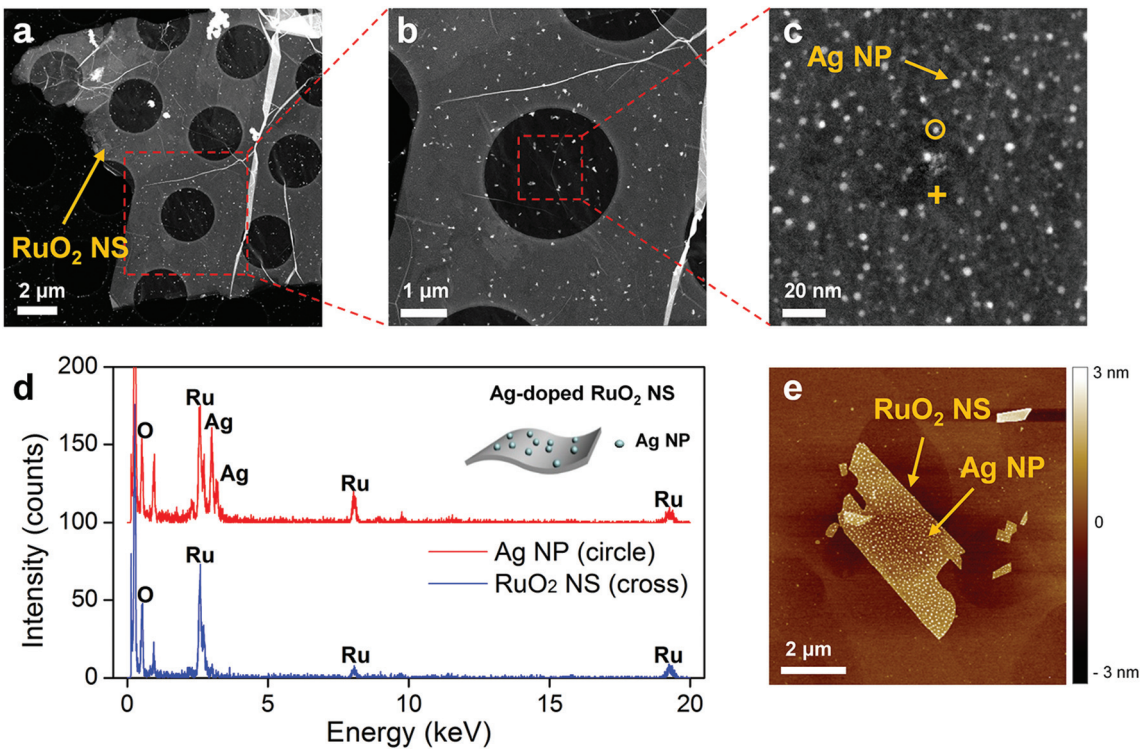

Fig. 2 (a), (b), and (c) TEM images of the Ag NPs decorated on the surface of RuO_2 NS, which produced the electrical doping effect of the pristine RuO_2 NS. (d) EDX pattern of the samples obtained from the TEM image. The two points on the Ag-doped RuO_2 NS (yellow cross and circle in (c) were examined. (e) Topographic AFM image of a Ag-doped RuO_2 NS dispersed on a Si/SiO_2 substrate.

 This journal is © The Royal Society of Chemistry 2017

Published on 28 April 2017. Downloaded by Yonsei University on 09/08/2017 07:25:42.

all the individual RuO_2 NS devices was measured by AFM, and the length and width of the channel were defined by FE-SEM after the electrical measurements.

LB-deposition and mechanical bending test

To utilize the monolayer RuO_2 NSs in LB-deposition, the RuO_2 NS colloidal suspension was centrifuged under the condition of 11 000 rpm for 30 minutes. Deionized water (210 ml) was carefully poured into the LB trough (KSV Instruments Ltd, MiniMicro LB System) and a diluted RuO_2 NSs colloidal suspension was gently placed on the surface of DI water using a syringe. After stabilizing for 10 min, the monolayer of RuO_2 NSs was compressed by the barriers at the speed of 10 mm min^{-1}. During the deposition, the surface pressure, which was provided by an observed microelectronic feedback system connected to Wilhelmy platinum plate, was controlled to be 12 mN m^{-1}. The deposition speed of the RuO_2 NSs on the PC substrates was 5 mm min^{-1}. The sheet resistance and optical transmittance of the RuO_2 NSs multilayer films on a PC substrate were characterized *via* an optical turbidity meter (NDH 7000SP, Nippon Denshoku, JP) and a non-contact resistance meter (EC-80P, Napson, JP), respectively. The cyclic bending test was carried out using an automatic bending tester (CFT-200R, Covotech Co., Ltd, KR).

Results and discussion

Enhancement of electrical conductivity in Ag-doped RuO_2 NSs

To examine this doping mechanism, individual RuO_2 NS devices were fabricated using electron beam lithography, and their electrical conductivity, carrier concentration, and mobility before and after Ag doping were measured. Fig. 3 shows a four-terminal device based on an individual RuO_2 NS and the electrical transport properties of the NSs. To determine the absolute resistance of the NS, transport properties were obtained using the four-probe technique without contact resistance between the NSs and the electrodes (Fig. 3a). The contact resistance was found to be two orders of magnitude less than that of the NSs, indicating ohmic contact. Fig. 3b shows the measured electrical conductivities (σ) of the pristine RuO_2 NS, the Ag-acetate-treated RuO_2 NS, and the Ag-doped RuO_2 NS at room temperature. Herein, two features were apparent: (i) the layer number-dependency of the conductivity and (ii) the effect of doping metal NPs on the conductivity.

As shown in Fig. 3c, the conductivities of the pristine NSs linearly increased with the increasing number of layers, indicating that the surface scattering of the carriers dominated the transport mechanism. If ℓ_b and ℓ_s were the mean free path of the bulk crystal and the surface scattering, respectively, the overall mean free path (ℓ) of the NSs was determined according to Matthiessen's rule: $1/\ell = 1/\ell_b + 1/\ell_s = 1/\ell_b + 1/\pi t$, where

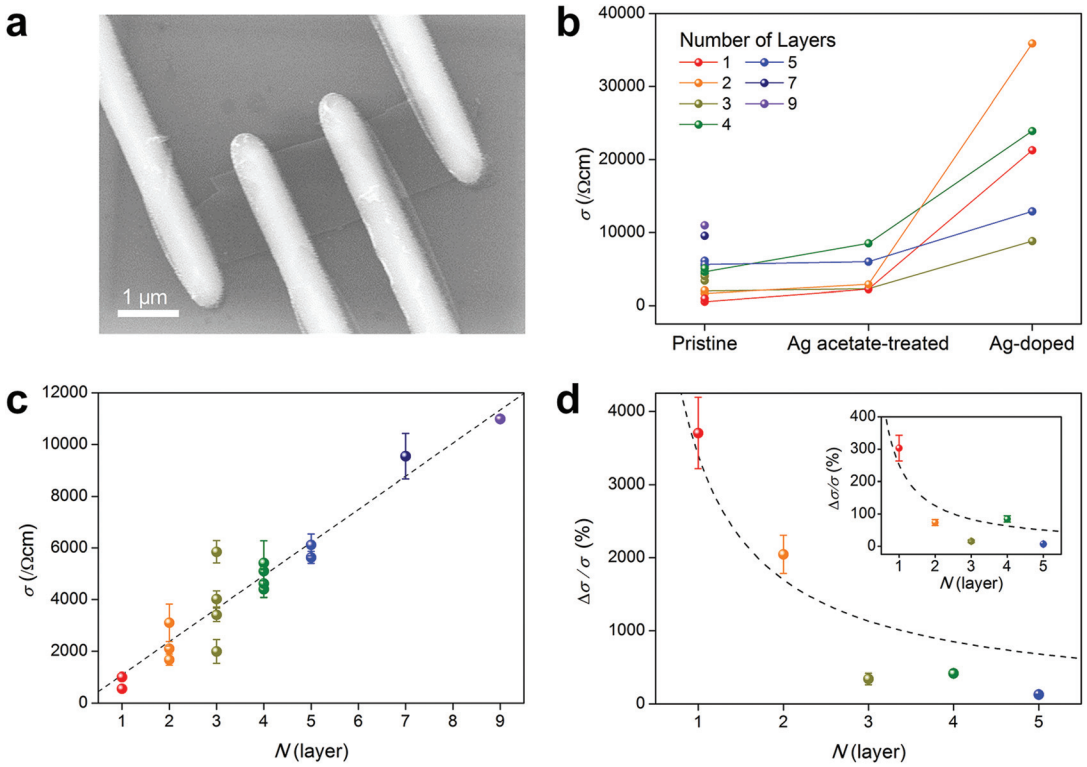

Fig. 3 Devices and electrical conductivity at room temperature. (a) SEM image of the 4-terminal device based on a single-crystalline RuO_2 NS. (b) Conductivity of the pristine, Ag-acetate-treated, and Ag-doped RuO_2 NS. (c) Conductivity of the pristine RuO_2 NS as a function of the number of layers. (d) Ag-doping effect on conductivity. The enhancement of conductivity is presented as $(\sigma_{Ag\text{-}doped} - \sigma_{pristine}) \times 100/\sigma_{pristine}$. The inset shows Ag-acetate-treated effect on conductivity, which is plotted as $(\sigma_{Ag\ acetate\text{-}treated} - \sigma_{pristine}) \times 100/\sigma_{pristine}$.

Published on 28 April 2017. Downloaded by Yonsei University on 09/08/2017 07:25:42.

t is the thickness of the NSs.[27] From this relation, the conductivity of the NS can be represented as follows:

$$\frac{\sigma}{\sigma_b - \sigma} = \frac{\pi}{\ell_b} \quad (1)$$

where σ_b is the conductivity of the bulk crystal. If the conductivity of the NS is significantly lower than that of the bulk crystal, the conductivity of the NS is linearly proportional to the thickness (number of layers). In the RuO_2 bulk crystals, the conductivity ($2.84 \times 10^4\ \Omega^{-1}\ cm^{-1}$) was found to be approximately 10 times higher than that measured in this study; thus, ℓ_b was calculated to be approximately 1 μm.[23,28] Our experimental results are thus in good agreement with the linear relation presented in eqn (1), as shown in Fig. 3c.

Note that the conductivity was enhanced by Ag doping (Fig. 3b). The conductivities of the Ag-doped NSs in particular dramatically increased by the $NaBH_4$ reduction process as compared to those of the pristine and Ag-acetate-treated NSs (red, orange, dark yellow, green, and blue lines). Furthermore, the change of electrical conductivities was not observed when the $NaBH_4$ reduction process was only carried out without Ag–acetate treatment, indicating that the doping effect was caused by the Ag NPs on the surface of the NSs (Table S1†). The doping effect on the conductivity *via* surface-treatment increased as the number of layers decreased, whereas the conductivity decreased as the number of layers decreased because of surface scattering. To obtain the layer number-dependent doping effect on conductivity, the mobility dependency due to the surface scattering was eliminated by normalization with the conductivity of the pristine NS, as shown in Fig. 3d. The enhancement of the conductivity dramatically increased with the decrease in the number of layers, reaching a maximum value of 3700% for the monolayer RuO_2 NS. If the carrier density of the pristine NS and the doping effect are n_i and n_d, respectively, the total number of carriers can be calculated as $N_i = wtLn_i$ and $N_d = wt_cLn_d$, respectively. Herein, w, t, L, *and* t_c are the width, thickness, length, and critical thickness affected by the doping effect, respectively. From this relation, the overall carrier density can be determined as $n = n_i + (t_c/t)n_d$. The enhancement of conductivity was then obtained by

$$\frac{\Delta\sigma}{\sigma} = \frac{t_c n_d}{n_i} \cdot \frac{1}{t}, \quad (2)$$

which indicates that the enhancement of conductivity was reciprocally proportional to the thickness of the NS (number of layers). Speculating that n_i, n_d, and t_c are constant in the RuO_2 NS, the enhancement of conductivity due to the doping effect was fitted with the number of layers according to eqn (2) (dashed line in Fig. 3d and inset). Because the critical thickness can be considered equal in both the Ag-acetate-treated and Ag-doped NSs, which was quantitatively confirmed *via* the Hall measurements, the induced carrier density in the Ag-doped NS was found to be more than 10 times of that in the Ag-acetate-treated NS. These interpretations based on the number of layers according to eqn (1) and (2) reveal that the mobility is dominated by the surface scattering and the surface treatment doping alters the carrier density.

These phenomena regarding the mobility and carrier density are consistent with the temperature-dependent conductivity, as shown in Fig. 4. Although the RuO_2 bulk crystals show metallic temperature-dependence of conductivity, RuO_2 NSs exhibit non-monotonic and semiconducting behaviors as the number of layers decreases, which can be observed in low-dimensional materials (Fig. 4a).[23,28,29] In a bulk crystal, the temperature dependence of conductivity is dominated by that of the mobility, which depends on the carrier–acoustic phonon scattering.[29] However, in a low-dimensional material such as a NS, the mobility is determined by the surface scattering rather than by the phonon scattering, as described in the interpretation using eqn (1). As a result, the thermal excitation of the carriers dominates the temperature dependence of the conductivity as a decrease of the dimension. For this reason, in the temperature range of 150–300 K, the metallic behavior clearly observed in the seven-layered NS was weakened in the four-layered NS, and the NSs with less than four-layers exhibited semiconducting behavior at all temperatures (inset of Fig. 4a). The exponentially reduced conductivity at temperatures below 100 K also revealed that the carrier

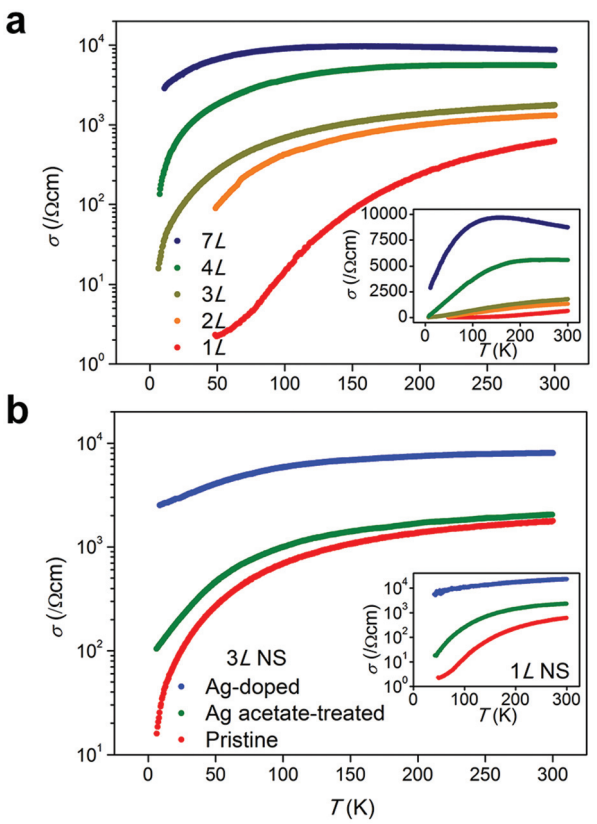

Fig. 4 Temperature-dependent electrical conductivity. (a) Conductivity of 1-, 2-, 3-, 4-, and 7-layered pristine RuO_2 NS. (b) Change of the temperature-dependent conductivity of 1- and 3-layered RuO_2 NSs according to the Ag-acetate treatment and Ag doping.

 This journal is © The Royal Society of Chemistry 2017

Published on 28 April 2017. Downloaded by Yonsei University on 09/08/2017 07:25:42.

density dominated the temperature dependence of the conductivity.

Fig. 4b and inset show the variation in the temperature dependence of the conductivity in pristine, Ag acetate-treated, and Ag-doped RuO_2 NSs. The carriers doped *via* Ag doping not only increased the conductivity but also reduced its temperature dependency, which indicated that the doped carrier density was retained even at low temperatures. In practice, the conductivity of the Ag-doped NS at 8.5 K is larger than that of the pristine NS at room temperature. The conductivity of NS before and after Ag doping can be expressed according to the carrier density as $\sigma_i = en_i\mu$ and $\sigma_d = e(n_i + n_d)\mu$, respectively. Using these relations and speculating that the change of the carrier mobility according to the doping process is negligible, the doped carrier density ratio between the Ag-doped NS and the Ag-acetate-treated NS was found to be 20.1 ± 3.1 at all temperatures. Consequently, the Ag-doping effect significantly increased the electrical conductivity at all temperatures, and the AgO_x formed on the surface of RuO_2 should be reduced to Ag NPs to considerably enhance the electrical conductivity.

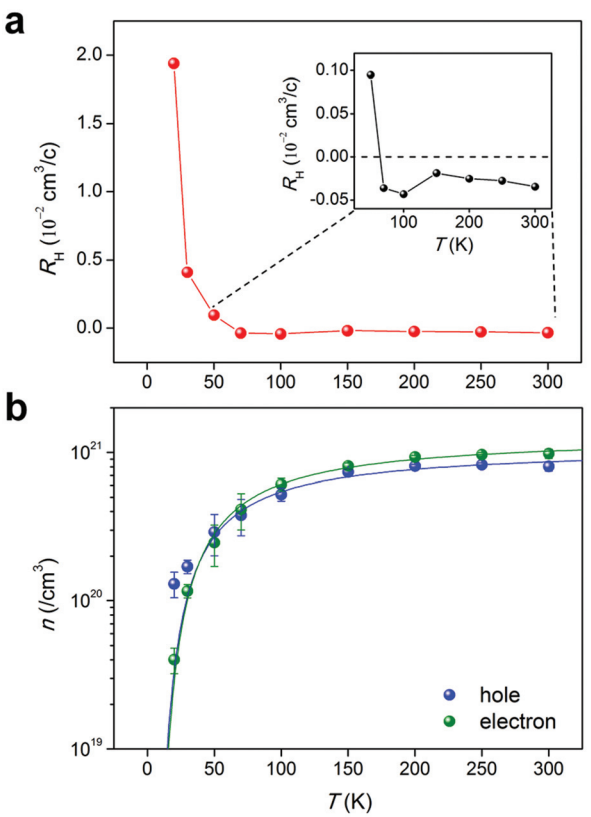

Fig. 5 Hall measurement and carrier density. (a) Hall coefficient of 4-layered pristine RuO_2 NS as a function of temperature. The inset shows the Hall coefficient within a range of 50–300 K. (b) Carrier densities of holes and electrons calculated from the Hall coefficient, which are fitted by the temperature dependence of the carrier density (solid lines).

To interpret the enhancement of electrical conductivity obtained by doping, Hall measurements were carried out using additional NS devices. Fig. 5a shows the variation of Hall coefficient in a four-layered pristine NS as a function of temperature. The variation ranging from negative to positive values indicates the ambipolar transport characteristics of the RuO_2 NS.[30,31] For the two-band system, in which electrons and holes coexist, the Hall coefficient (R_H) is determined by the partial Hall coefficients of each carrier weighted by the square of their partial conductivities.[32,33] Therefore, for the pristine RuO_2 NS, the total Hall coefficient is given by

$$R_H = \frac{\sigma_h^2 R_{H,h} + \sigma_e^2 R_{H,e}}{(\sigma_h + \sigma_e)^2} = \frac{\mu_h^2 p - \mu_e^2 n}{e(\mu_h p + \mu_e n)^2}, \quad (3)$$

where the subscripts h and e mean holes and electron, respectively. Because the partial Hall coefficients of electrons and holes exhibit opposite signs, the total Hall coefficient of the two-band system is significantly smaller than the partial Hall coefficients. Moreover, it is difficult to obtain the carrier density from the measured total Hall coefficient due to this offset. On the other hand, for a Ag-doped RuO_2 NS, in which the major carrier is electrons, the carrier density can be obtained using a simple relation, $R_H = -1/ne$. In the Ag-doped NS, the carrier density and mobility were found to be 2.56×10^{21} cm^{-3} and 17.7 cm^2 V^{-1} s^{-1}, respectively, which are reasonable values as compared to those reported in a previous study.[34] The small mobility of RuO_2 NSs can be attributed to the surface scattering caused by the significant spatial confinement of the NS structure, as shown in Fig. 3c. From the Matthiessen's rule, the mean free path of the four-layered NSs was found to be 13.6 nm, which was two orders of magnitude smaller than that of the bulk. Therefore, it can be considered that the carrier mobility, which is significantly restricted by the NS structure, cannot be affected by doping. If we consider that the mobility of holes is similar to that of the electrons, it is possible to find the variation of carrier density in both the holes and electrons using the two equations $\sigma = e(\mu_h p + \mu_e n)$ and eqn (3). Table 1 summarizes the obtained transport properties. The Ag doping increases the electron density and decreases the hole density. From the obtained variation of carrier density, the critical thickness affected by doping was found to be approximately 1 nm in the case of both the Ag-acetate-treated and Ag-doped NSs according to eqn (2).

Similarly, the temperature dependency of the carrier density can be estimated using the measured Hall coefficients

Table 1 Variations of properties according to the doping process

Properties	Pristine	Ag-acetate-treated	Ag-doped
R_H (cm^3 c^{-1})	-2.93×10^{-3}	-3.89×10^{-3}	-2.44×10^{-9}
σ (Ω cm)	3240	3540	7260
p (cm^{-3})	2.65×10^{20}	1.38×10^{20}	—
n (cm^{-3})	8.79×10^{20}	1.11×10^{21}	2.56×10^{21}

Published on 28 April 2017. Downloaded by Yonsei University on 09/08/2017 07:25:42.

(Fig. 5b). The densities of the electrons and holes were determined by the relations

$$n = N_c \exp\left(-\frac{E_c - E_F}{kT}\right) \quad (4)$$

and

$$p = N_v \exp\left(-\frac{E_F - E_v}{kT}\right), \quad (5)$$

respectively.[27] Herein, N, E, and k indicate the effective densities of state, band energy, and Boltzmann constant, respectively, and the subscripts c, v, and F represent the conduction and valence band edges and Fermi energy, respectively. The estimated electron and hole densities were fitted using eqn (4) and (5), and the effective densities of state of electrons and holes were found to be 1.33×10^{21} cm^{-3} and 1.09×10^{21} cm^{-3}, respectively. From the fitting, the overlap energy between the conduction and valence bands was found to be approximately 12.0 meV. This small band overlap energy indicates semi-metallic characteristics in the RuO_2 NSs.

Flexible transparent electrode films of the Ag-doped RuO_2 NSs

The Langmuir–Blodgett (LB) method, which had advantages in the deposition of self-assembled monolayer films, was employed for the fabrication of the flexible transparent electrode on polycarbonate (PC) substrates. A diluted RuO_2 NSs colloidal suspension with a density of 5 μg cm^{-3} was utilized, and the surface pressure of the air–water interface was controlled to increase the packing density of RuO_2 NSs. The detailed condition of the LB deposition has been discussed in the experimental methods. Prior to doping Ag NPs on the RuO_2 NSs, the pristine RuO_2 NSs were deposited. Fig. 6a shows that the pristine RuO_2 NSs were deposited in a monolayer, such that the packing density of the pristine RuO_2 NSs was calculated to be about 89% from the SEM image (inset of Fig. 6a). Therefore, to obtain sufficient electrical path in the films, the LB deposition process should be adequately repeated for good coverage of the films. After the LB deposition, ultra-violet (UV) irradiation cleaning was carried out to remove tetrabutylammonium ions and make the surface hydrophilic. For enhancing the electrical conductivity of the LB-deposited films, Ag doping on the RuO_2 NSs was utilized by dipping pristine RuO_2 NSs in 0.05 M Ag-acetate solution and 0.05 M $NaBH_4$ solution in sequence as abovementioned. Ag NPs were successfully formed on the LB-deposited film, as verified in Fig. 6b. To investigate the cross-sectional nanoscale structure of the multilayer films, LB deposition of the Ag-doped RuO_2 NSs was carried out on the Si substrate using the same process. HR-TEM image, as shown in Fig. 6c, indicated that the LB-deposited Ag-doped RuO_2 films have a relatively uniform structure with a total thickness of ~7 nm.

For revealing the layer number-dependent doping effect in the RuO_2 NSs films, the electrical and optical properties of the LB-deposited films with various number of LB depositions and Ag doping conditions were investigated. Table 2 shows the LB-deposition and Ag doping conditions of the samples. It was not possible to measure the electrical properties of the two-layer film since the electrical path was not established due to the voids between NSs (Fig. S2†). As shown Fig. 6d, the sheet

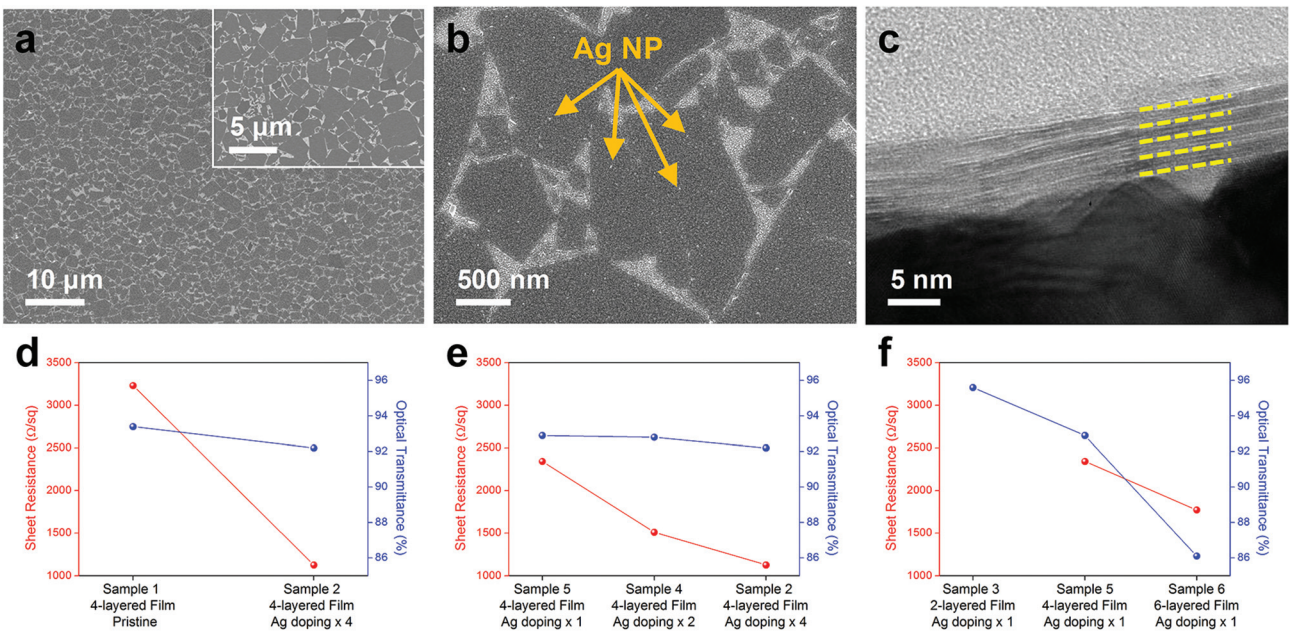

Fig. 6 LB-deposited RuO_2 NSs films on a PC film. (a) SEM image of the pristine RuO_2 NSs monolayer film by LB-deposition. The packing density of the RuO_2 NSs was calculated from the SEM image of the inset. (b) SEM image of the Ag-doped RuO_2 NSs monolayer film. (c) The cross-sectional TEM image of the nanoscale lamellar structure in the LB-deposited RuO_2 NSs multilayer film (4-layer). The sheet resistance and optical transmittance of the RuO_2 NSs multilayer films as a fucntion of (d), (e) Ag doping condition, and (f) the number of the LB-layer.

 This journal is © The Royal Society of Chemistry 2017

Published on 28 April 2017. Downloaded by Yonsei University on 09/08/2017 07:25:42.

Table 2 LB-deposition and Ag doping conditions of the samples

Sample No.	LB-deposition and Ag doping	Layer no.
Sample 1	LB-deposition × 4	4
Sample 2	(LB-deposition + Ag doping) × 4	4
Sample 3	LB-deposition × 2 + Ag doping	2
Sample 4	(LB-deposition × 2 + Ag doping) × 2	4
Sample 5	LB-deposition × 4 + Ag doping	4
Sample 6	LB-deposition × 6 + Ag doping	6

resistance and optical transmittance of the Ag-doped RuO_2 NS four-layer films were measured to be ~1.1 kΩ sq^{-1} and ~92.2% in the visible region. Considering that the sheet resistance and optical transmittance of the pristine RuO_2 NSs multilayer films with the same number of layers were found to be ~3.2 kΩ sq^{-1} and ~93.4%, it was proven that the Ag doping was effective for enhancing the electrical transport of the pristine RuO_2 NS multilayer films. This result obtained for the LB-deposited RuO_2 films is consistent with that obtained for an individual NS, as shown in Fig. 4b. Note that the change in optical transmittance was almost negligible before and after Ag-doping, whereas the reduction of sheet resistance was remarkably high. The negligible degradation of the optical transmittance in Ag-doped RuO_2 NSs multilayer films can be attributed to the extremely small diameter of the Ag NPs (~2 nm), which is too small to scatter the light of the visible region.

Fig. 6e shows the Ag doping condition dependences in the four-layer films. On increasing the number of doping processes, the sheet resistance was considerably reduced, whereas the transmittance was negligibly reduced. On the other hand, the optical transmittance was significantly decreased with the increasing number of the LB layer (Fig. 6f).

Since the main objective of using a flexible electrode is to realize the reliable performance from the continuous mechanical deformation, the mechanical stability was tested using the fabricated Ag-doped RuO_2 NS multilayer films (Sample 2, 4, and 6). Fig. 7a shows the schematic of the continuous bending test. The bending angle and bending radius were set at 180 degrees and 1 mm, respectively. The resistance of the films was measured *in situ* when the bending test was carried out. The Ag-doped RuO_2 NSs multilayer films (Sample 2) demonstrated extraordinarily high bending stability, showing that the change of the resistance ($\Delta R/R_0$) was less than 1% over 50 000 cycles. Moreover, $\Delta R/R_0$ is ~9% over 200 000 cycles. The $\Delta R/R_0$ of Sample 4 has a value similar to that of Sample 2, whereas the $\Delta R/R_0$ of Sample 6 shows a higher change in the resistance of ~12%. Considering that the $\Delta R/R_0$ of the Ag nanowires, which are very commercial materials for transparent flexible electrodes, is ~50% at 2000 cycles in the bending radius of 1 mm, it is clear that RuO_2 NSs films could improve the bending stability because of the thinner film thickness of the Ag-doped RuO_2 NS multilayer films.[35] As shown in Fig. S3,† the Ag-doped RuO_2 NSs multilayer films were not delaminated from the substrate although small degradation was observed. To examine the foldability and the electrical connectivity, light emitting diode (LED) bulbs were connected to the Ag-doped

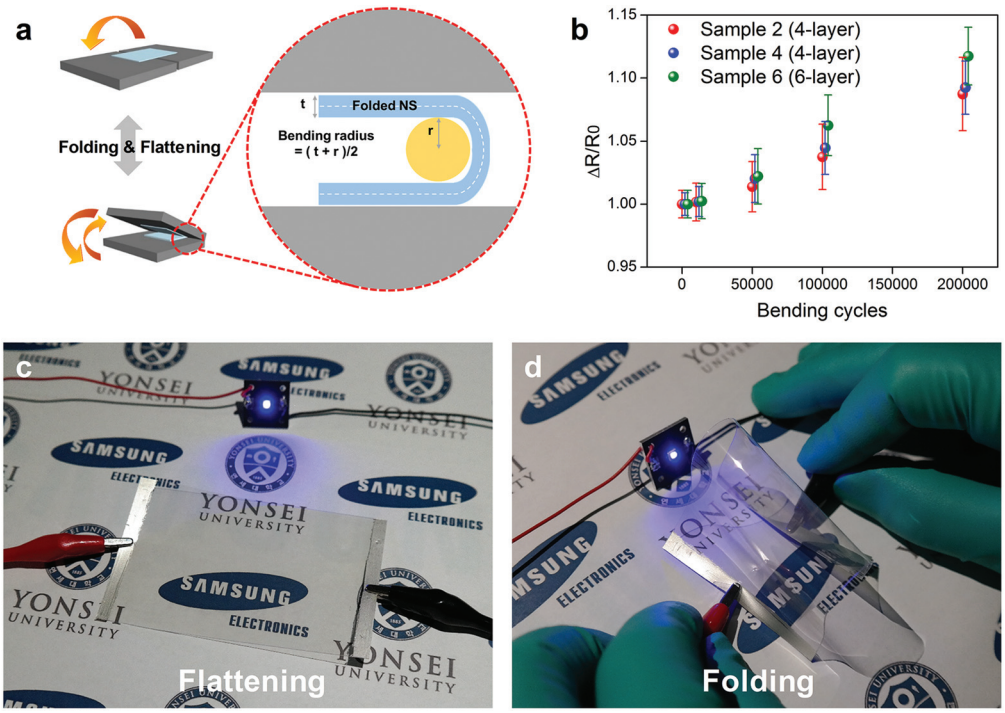

Fig. 7 (a) Schematic of the continuous bending test (bending radius = 1 mm). (b) The change in the resistance for Ag-doped RuO_2 NS multilayer films on a PC substrate during the cyclic bending test. (c) and (d) Images of the blue LED connected to the Ag-doped RuO_2 NS multilayer films on a PC substrate under the condition of flattening and folding, respectively.

Published on 28 April 2017. Downloaded by Yonsei University on 09/08/2017 07:25:42.

RuO_2 NS multilayer films on a PC substrate. The light of the LED remained turned on, as shown in Fig. 7c, when the Ag-doped RuO_2 NSs multilayer films were folded.

Conclusions

In summary, we systemically investigated the electrical transport properties in the exfoliated individual RuO_2 NSs. It was revealed that Ag doping by the decoration of Ag NPs on the surface of the RuO_2 NSs was effective to enhance the electrical conductivity of the RuO_2 NSs. In particular, the electrical conductivity of a monolayer RuO_2 NS was increased by up to 3700%. The enhanced electrical conductivity *via* Ag doping increased with the decreasing number of layers, indicating the clear layer-number dependence. This result obviously shows that the mobility is dominated by surface scattering and the carrier density of RuO_2 NSs is increased *via* Ag doping. Our results demonstrate that the Ag NP doping and layer number of NS play very significant roles in the charge transport of the RuO_2 NSs. Furthermore, the Ag-doped RuO_2 NS multilayer films show an extraordinarily high bending stability that the change in the resistance is less than 1% over 50 000 cycles, with a reduced sheet resistance of one-third. These enhanced electrical properties and mechanical stability of the Ag-doped RuO_2 NSs multilayer films suggest the application of 2D oxide materials as nanoscale transparent electrodes for the flexible electronics and optoelectronics.

Author contributions

W. L. and J. W. R. designed and directed the research; S. Y., J. K., H. M., J. W. R., and W. L. performed the research; S. Y., J. K., H. M., S. Y. K., D. K., W. H. S., S. H., D. W. J., S. S., C. K., J. W. R., and W. L. analyzed the data; and S. Y., J. K., J. W. R., and W. L. wrote the paper.

Acknowledgements

This work was supported by the National Research Foundation of Korea (NRF) Grant funded by the Korea government (MSIP) (2014R1A2A1A10053869) and the Priority Research Centers Program (2009-0093823).

References

1 Y. Zhang, Y.-W. Tan, H. L. Stormer and P. Kim, *Nature*, 2005, **438**, 201–204.
2 K. S. Novoselov, A. K. Geim, S. V. Morozov, D. Jiang, Y. Zhang, S. V. Dubonos, I. V. Grigorieva and A. A. Firsov, *Science*, 2004, **306**, 666–669.
3 M. Osada and T. Sasaki, *Adv. Mater.*, 2012, **24**, 210–228.
4 Q. H. Wang, K. Kalantar-Zadeh, A. Kis, J. N. Coleman and M. S. Strano, *Nat. Nanotechnol.*, 2012, **7**, 699–712.
5 J. A. Wilson, F. J. Di Salvo and S. Mahajan, *Phys. Rev. Lett.*, 1974, **32**, 882–885.
6 A. Cao, Z. Liu, S. Chu, M. Wu, Z. Ye, Z. Cai, Y. Chang, S. Wang, Q. Gong and Y. Liu, *Adv. Mater.*, 2010, **22**, 103–106.
7 H. Zhang, S. B. Lu, J. Zheng, J. Du, S. C. Wen, D. Y. Tang and K. P. Loh, *Opt. Express*, 2014, **22**, 7249–7260.
8 G.-H. Lee, Y.-J. Yu, X. Cui, N. Petrone, C.-H. Lee, M. S. Choi, D.-Y. Lee, C. Lee, W. J. Yoo, K. Watanabe, T. Taniguchi, C. Nuckolls, P. Kim and J. Hone, *ACS Nano*, 2013, **7**, 7931–7936.
9 Q. Peng, Z. Wang, B. Sa, B. Wu and Z. Sun, *ACS Appl. Mater. Interfaces*, 2016, **8**, 13449–13457.
10 Q. He, Z. Zeng, Z. Yin, H. Li, S. Wu, X. Huang and H. Zhang, *Small*, 2012, **8**, 2994–2999.
11 K. Watanabe, T. Taniguchi and H. Kanda, *Nat. Mater.*, 2004, **3**, 404–409.
12 B. Radisavljeviz, A. Radenovic, J. Brivio, V. Giacometti and A. Kis, *Nat. Nanotechnol.*, 2011, **6**, 147–150.
13 Y. Zhang, T.-R. Chang, B. Zhou, Y.-T. Cui, H. Yan, Z. Liu, F. Schmitt, J. Lee, R. Moore, Y. Chen, H. Lin, H.-T. Jeng, S.-K. Mo, Z. Hussain, A. Bansil and Z.-X. Shen, *Nat. Nanotechnol.*, 2014, **9**, 111–115.
14 D. Voiry, H. Yamaguchi, J. Li, R. Silva, D. C. B. Alves, T. Fujita, M. Chen, T. Asefa, V. B. Shenoy, G. Eda and M. Chhowalla, *Nat. Mater.*, 2013, **12**, 850–855.
15 N. E. Staley, J. Wu, P. Eklund, Y. Liu, L. Li and Z. Xu, *Phys. Rev. B: Condens. Matter Mater. Phys.*, 2009, **80**, 184505.
16 J. Demsar, L. Forró, H. Berger and D. Mihailovic, *Phys. Rev. B: Condens. Matter Mater. Phys.*, 2002, **66**, 041101.
17 C. Chiritescu, D. G. Cahill, N. Nguyen, D. Johnson, A. Bodapati, P. Keblinski and P. Zschack, *Science*, 2007, **315**, 351.
18 J. Tao, T. Luttrell and M. Batzill, *Nat. Chem.*, 2011, **3**, 296–300.
19 Y. Chen, D. Ye, M. Wu, H. Chen, L. Zhang, J. Shi and L. Wang, *Adv. Mater.*, 2014, **26**, 7019–7026.
20 X. Rui, Z. Lu, Z. Yin, D. H. Sim, N. Xiao, T. M. Lim, H. H. Hng, H. Zhang and Q. Yan, *Small*, 2013, **9**, 716–721.
21 R. Ma and T. Sasaki, *Acc. Chem. Res.*, 2015, **48**, 136–143.
22 L. F. Mattheiss, *Phys. Rev. B: Condens. Matter Mater. Phys.*, 1976, **13**, 2433–2450.
23 W. D. Ryden, A. W. Lawson and C. C. Sartain, *Phys. Rev. B: Condens. Matter Mater. Phys.*, 1970, **1**, 1494–1500.
24 J. Sato, H. Kato, M. Kimura, K. Fukuda and W. Sugimoto, *Langmuir*, 2010, **26**, 18049–18054.
25 C. Wang, M. Osada, Y. Ebina, B.-W. Li, K. Akatsuka, K. Fukuda, W. Sugimoto, R. Ma and T. Sasaki, *ACS Nano*, 2014, **8**, 2658–2666.
26 R. R. Nair, P. Blake, A. N. Grigorenko, K. S. Novoselov, T. J. Booth, T. Stauber, N. M. R. Peres and A. K. Geim, *Science*, 2008, **320**, 1308–1308.
27 S. O. Kasap, *Principles of Electronic Materials and Devices*, McGraw-Hill, 2006.

 This journal is © The Royal Society of Chemistry 2017

28 W. D. Ryden, A. W. Lawson and C. C. Sartain, *Phys. Lett. A*, 1968, **26**, 209–210.
29 J. Kim, S. Lee, Y. M. Brovman, P. Kim and W. Lee, *Nanoscale*, 2015, **7**, 5053–5059.
30 K. Y. Tong, V. Jelenkovic, W. Y. Cheung and S. P. Wong, *J. Mater. Sci. Lett.*, 2001, **20**, 699–700.
31 M. M. Steeves and R. J. Lad, *J. Vac. Sci. Technol., A*, 2010, **28**, 906–911.
32 N. W. Ashcroft and N. D. Mermin, *Solid State Physics*, BROOKS/COLE CENGAGE Learing, 1976.
33 S. O. Kasap, *Hall effect in semiconductors*, Web-Materials, 2001.
34 M. S. Osofsky, C. M. Krowne, K. M. Charipar, K. Bussmann, C. N. Chervin, I. R. Pala and D. R. Rolison, *Sci. Rep.*, 2016, **6**, 21836.
35 J.-H. Kim and J.-W. Park, *ACS Appl. Mater. Interfaces*, 2015, **7**, 18574–18580.

Published on 28 April 2017. Downloaded by Yonsei University on 09/08/2017 07:25:42.